Large-Area, Freestanding, Single-Layer Graphene–Gold: A Hybrid Plasmonic Nanostructure

Ganjigunte R. Swathi Iyer,[†,*] Jian Wang,[†] Garth Wells,[†] Srinivasan Guruvenket,[‡] Scott Payne,[§] Michael Bradley,[⊥] and Ferenc Borondics[†,*]

[†]Canadian Light Source, 44 Innovation Boulevard, Saskatoon, SK S7N 2V3, Canada, [‡]Centre for Nanoscale Science and Engineering (CNSE) and [§]Electron Microscopy Center, North Dakota State University, Fargo, North Dakota 58102, United States, and [⊥]Department of Physics and Engineering Physics, University of Saskatchewan, Saskatoon, SK S7N 5E2, Canada

ABSTRACT

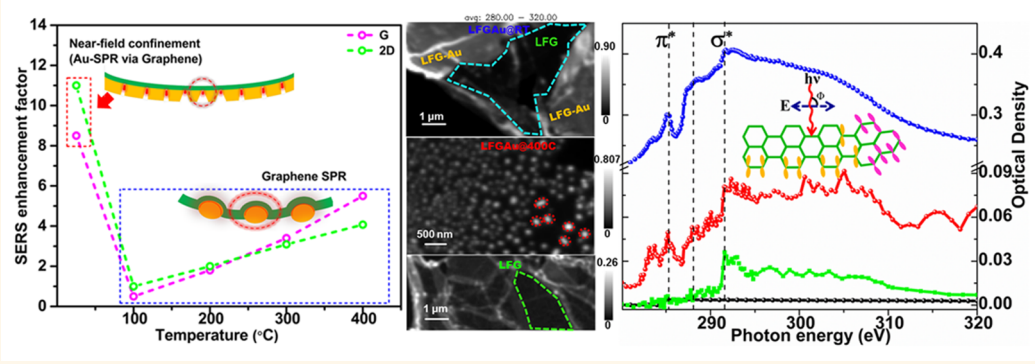

Graphene-based plasmonic devices have recently drawn great attention. However, practical limitations in fabrication and device architectures prevent studies from being carried out on the intrinsic properties of graphene and their change by plasmonic structures. The influence of a quasi-infinite object (*i.e.*, the substrate) on graphene, being a single sheet of carbon atoms, and the plasmonic device is overwhelming. To address this and put the intrinsic properties of the graphene–plasmonic nanostructures in focus, we fabricate large-area, freestanding, single-layer graphene–gold (LFG-Au) sandwich structures and Au nanoparticle decorated graphene (formed *via* thermal treatment) hybrid plasmonic nanostructures. We observed two distinct plasmonic enhancement routes of graphene unique to each structure *via* surface-enhanced Raman spectroscopy. The localized electronic structure variation in the LFG due to graphene–Au interaction at the nanoscale is mapped using scanning transmission X-ray microscopy. The measurements show an optical density of ~0.007, which is the smallest experimentally determined for single-layer graphene thus far. Our results on freestanding graphene–Au plasmonic structures provide great insight for the rational design and future fabrication of graphene plasmonic hybrid nanostructures.

KEYWORDS: SERS · freestanding graphene · STXM · NEXAFS · plasmonics

Graphene, a single sheet of sp^2-hybridized carbon atoms with zero band gap and a linear $E = E(k)$ relationship for both electrons and holes,[1,2] owing to its excellent tunable electronic and optical properties has great potential for many nano- and optoelectronics applications.[3] Recently, there has been overwhelming research interest in graphene plasmonics.[4−10] While tuning of graphene plasmons by electrostatic gating for optoelectronic devices has drawn great attention,[11−15] the well-established Raman features[16] and various properties such as doping,[17−19] effect of various substrates,[20,21] stress–strain,[22−26] and defects[27] in graphene *via* Raman spectroscopy have best exemplified the importance of graphene as a surface-enhanced Raman spectroscopy (SERS) substrate.[28−35]

Traditionally in SERS, surface interactions between the incident electromagnetic radiation and surface plasmons of nanostructures are detected at the metal–dielectric interfaces. Graphene as a SERS substrate has been realized by integrating it with

* Address correspondence to Swathi.Iyer@lightsource.ca, Ferenc.Borondics@lightsource.ca.

Received for review April 4, 2014 and accepted May 26, 2014.

Published online May 26, 2014
10.1021/nn501864h

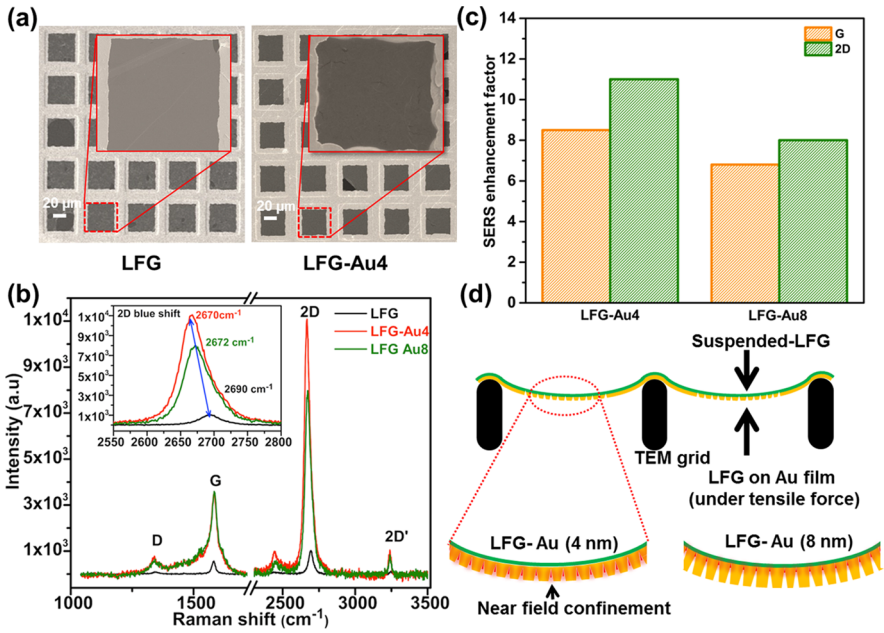

Figure 1. (a) Scanning electron microscopy (SEM) micrographs of the pristine, large-area, freestanding SLG (LFG) (left) and LFG-Au4 film (right) transferred onto a transmission electron microscopy (TEM) grid. (Inset) Magnified view of a single mesh, respectively. (b) Overlay Raman spectra of LFG, LFG-Au4, and LFG-Au8 (inset) of the magnified 2D spectra. (c) Calculated enhancement factor (EF) of the G and 2D bands for LFG-Au4 and LFG-Au8 films. (d) Schematics of the near-field confinement in LFG-Au4 and LFG-Au8 films.

(i) well-defined arrays of gold (Au) nanodisks,[28] Au pyramids,[35] photonic nanocrystal nanocavities,[36] and localized nanocavities between Au metal particles;[34] (ii) deposition of Au on Si/SiO_2/graphene multilayer systems by varying the number of graphene layers; and (iii) thermally assisted self-assembled Ag nanoparticles on graphene[33] as well as graphene-veiled Au nanoparticles, all of which are supported on Si/SiO_2 substrates.[31] Importantly, being a single sheet of carbon atoms, the supporting substrate is known to play a vital role in influencing graphene's electronic and mechanical properties.[20,21] In graphene supported on a Si/SiO_2 substrate, the interference in the SiO_2 layer enhances field amplitudes within graphene, resulting in enhanced Raman signal.[37−39] Therefore, the plasmonic properties of metal nanostructures formed on graphene are greatly influenced by the supporting substrate as well.[28,31,33−35] A freestanding geometry eliminates the strong substrate influence and provides a different geometry for fundamental studies of the intrinsic properties of such systems, leading to unique sensing applications. However, due to difficulties with obtaining large-area freely suspended single-layer graphene, a limited amount of research has been focused toward this direction.[25,26,40,41]

In this article, we report a simple two-step approach to fabricate large-area freestanding graphene−gold (LFG-Au) nanostructures. The plasmonic activity and localized metal−graphene interactions at the nanoscale of the devices are investigated. The SERS of the as-prepared LFG-Au structure shows a 9-fold and 6-fold enhancement at the 2D and G band due to the localized surface plasmon confinement in nanocracks formed in the freestanding Au film. LFG-Au plasmonic nanostructures are fabricated by coupling graphene with the underlying self-assembled array of Au nanoparticles formed by thermal disintegration of the Au film. The electronic corrugations in graphene due to the localized graphene surface plasmon−metal interactions, mapped at the nanoscale using scanning transmission X-ray microscopy (STXM), a spatially resolved synchrotron-based spectro-microscopic technique, are reported for the first time. Additionally, the experimentally determined optical density (OD) of ~0.007 for the single-layer graphene (SLG), closely matching theoretical calculations[42,43] (see Supporting Information), elucidates the thinnest graphene measured thus far.

RESULTS AND DISCUSSION

Near-Field Confinement in LFG-Au Film. Figure 1a shows the scanning electron microscopy (SEM) image of large-area graphene samples with (right) and without (left) underlying Au film suspended on a TEM grid (3 mm, 400 mesh SPI, 433HG-CF). The insets in both images are enlarged section of an individual mesh ($40 \times 40\ \mu m$). For convenience, we refer to the pristine freestanding SLG as large-area freestanding graphene (LFG) and the LFG with 4 and 8 nm thick Au film as LFG-Au4 and LFG-Au8, respectively. The morphology of LFG films shows the characteristic smooth surface of graphene, while that of LFG-Au4 shows nano- and micro-sized cracks over the entire surface. Figure 1b shows the Raman spectra of LFG (black) and SERS spectra of

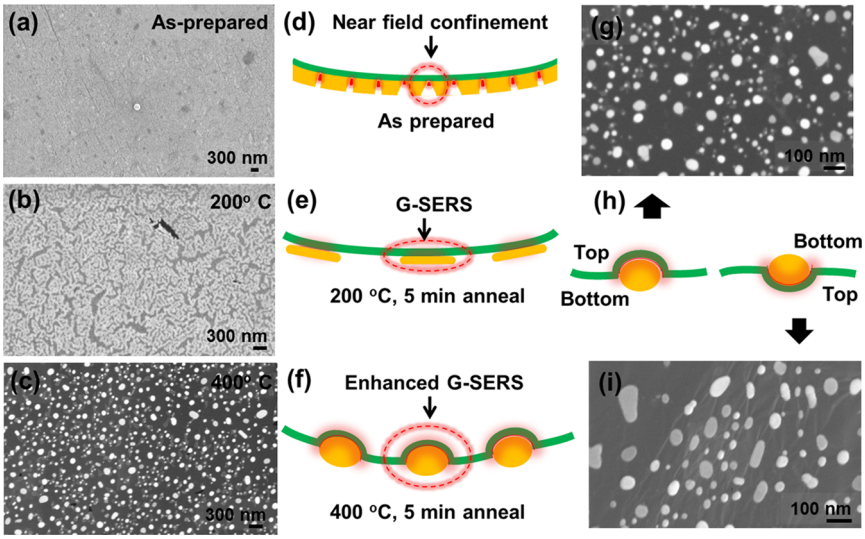

Figure 2. SEM micrographs of LFG-Au4 samples as a function of annealing temperature: (a–c) As-prepared, annealed at 200 and 400 °C. (d–f) Schematic of microstructural transformation with heat treatment. (g, i) Top and bottom view of magnified SEM micrograph of LFG-Au4 @400 °C. (h) Schematics representing the top and bottom view of LFG-AuNPs.

LFG-Au4 (red) and LFG-Au8 (green) samples with the inset showing zoomed graphs of the 2D band. The spectra show two prominent Raman bands, the G (1582 cm^{-1}) and 2D (2690 cm^{-1}) band, with a low-intensity D band at 1350 cm^{-1}, typical of freestanding SLG.[44] Compared to LFG, all the Raman bands in the LFG-Au4 and LFG-Au8 exhibit significant enhancement. The positions and symmetric line shapes of both G and 2D bands in LFG samples indicate that they are undoped with little disorder and negligible native strain.[24] Recently, Raman studies on strain sensitivity of graphene have shown that the tensile strain results in softening phonon modes.[25,26] While the position of the G band for LFG-Au films remains unchanged, the fwhm increases (24 cm^{-1}). The 2D bands of LFG-Au are significantly red-shifted, *i.e.*, LFG-Au4 by 20 cm^{-1} and LFG-Au8 by 18 cm^{-1} (Figure 1b inset), compared to the LFG, indicating a biaxial strain in the graphene film after Au deposition akin to intentionally pressurized graphene bubbles.[25] The unaltered position along with line broadening of the G band and significant red-shift in the 2D band are in agreement with previous studies that have shown higher strain sensitivity of the 2D band compared to the G band.[22,23,45] There is no splitting of the 2D band in the LFG-Au samples; it becomes asymmetric along with an increase in the peak width (30 cm^{-1}). Heeg *et al.* observed a similar red-shift in addition to splitting of the 2D band in graphene suspended between two Au disks, separated by 30 nm, on a SiO_2 substrate.[34]

The intensities of the Raman bands for the LFG-Au samples are significantly enhanced compared to the LFG samples, displaying SERS. The enhanced intensities are evaluated by the enhancement factor (EF), defined as the ratio of corresponding peak intensities of plasmonic graphene and pristine graphene. The calculated EF of the G and 2D bands are 9 and 11 for the LFG-Au4 and 7 and 8 for LFG-Au8, respectively (shown in Figure 1c). The biaxial strain in the suspended graphene-Au stack creates nanocracks in the LFG-Au films due to differences in the elastoplastic properties of graphene and gold.[46] These nanometer-sized cracks in the Au film (see Supporting Information Figure S1b) act as near-field confinement zones and play a significant role in the enhancement of the Raman signal of graphene (*i.e.*, SERS effect). The nanocracks in the Au films are wedge shaped due to the bowing effect of the suspended graphene membrane as schematically illustrated in Figure 1d for both LFG-Au4 and LFG-Au8 films. An increase in Au film thickness creates additional downward force, leading to more bowing, resulting in further opening of the cracks in the Au film, but still retaining the wedge shape. However, this significantly decreases the near-field confinement and ultimately leads to decreased EF.

Graphene Surface Plasmon Resonators. The plasmonic nanostructures have been realized by thermally assisted fragmentation of homogeneous metal thin films into nanoparticles (NPs). The near-field confinement in such NPs is known to depend on their size, morphology, and interparticulate separation.[47] Graphene has been widely used as a sensing material to study the plasmonic activity in these structures *via* SERS. In this study, the as-prepared LFG-Au samples are annealed at various temperatures in Ar atmosphere to form self-assembled AuNPs, which couple with LFG to form LFG-Au plasmonic nanostructures. A comparative depiction of the large-area graphene before and after annealing is shown in Supporting Information S1(a–d).

Figure 2a–c depicts SEM images of as-prepared LFG-Au4 and LFG-Au4 subjected to 200 and 400 °C annealing temperatures. Figure 2d–f is a schematic

illustration of the LFG-Au4 film's transformation upon annealing. Annealing at 200 °C shows wider cracks in the Au film. Increasing the temperature to 300 °C leads to formation of wirelike strands, which on further annealing (400 °C) transforms into spherical shaped NPs. The NPs are mostly circular, with their sizes ranging from 30 to 300 nm and average diameter of 50 nm. The size and shape of AuNPs show a dependence on the Au film thickness. The 4 nm Au film visibly breaks into particulates at 400 °C, while the 8 nm Au film at the same temperature fragments into elongated, irregularly shaped NPs with an average diameter larger than 200 nm. The morphological transformation of LFG-Au8 films subjected to different annealing temperatures is presented in Supporting Information S2(a−c).

Since the AuNPs are mostly formed in the LFG-Au4 films annealed at 400 °C, we consider these films particularly interesting to understand the localized interfacial interaction between the LFG and Au. Figures 2g,i, depicting the magnified images of Figure 2c, present a deeper insight of the self-assembled AuNPs and the overlying LFG. Since the samples in this study are freestanding, they provide the advantage of investigating it from both sides, which has not been possible for graphene supported on a substrate. The LFG film wrapped around these smaller AuNPs in such a fashion to create wrinkles at the edges of the particles, further elucidated with the HRTEM images shown in Supporting Information S3. It is strikingly interesting that the wrinkling is all along the same direction and seems to be stitched together to the next closest particle. From the top view (Figure 2g), the LFG over the AuNPs is comparable to a thin linen cloth sheet (≅LFG) conforming to a pack of scattered golf balls (≅AuNPs) (also see Supporting Information Figure S4). From the bottom view (Figure 2i), each AuNP makes a localized depression in the LFG film similar to golf balls pressing into a thin linen cloth. From both the top and bottom view it is obvious that the LFG conforms (partially) around these AuNPs, as illustrated in the schematic, Figure 2h.

Thin solid metal films deposited on a substrate are generally metastable and upon heating can fragment or agglomerate *via* the dewetting process. In general, dewetting depends on the film thickness and the surface energy and is driven by the energy minimization principle. As put forth by Thompson *et al.*, dewetting occurs in three steps: hole formation, hole growth and impingement, and ligament breakup.[46] The formation of AuNPs in our case involves similar steps and is schematically illustrated in Figure 2d−f. The difference in the thermal and elastoplastic properties of graphene and Au creates internal strain (this occurs during the film-growth process). Upon suspending the LFG-Au layers on a TEM grid, the bowing of graphene-Au creates additional strain, leading to nanocracks in

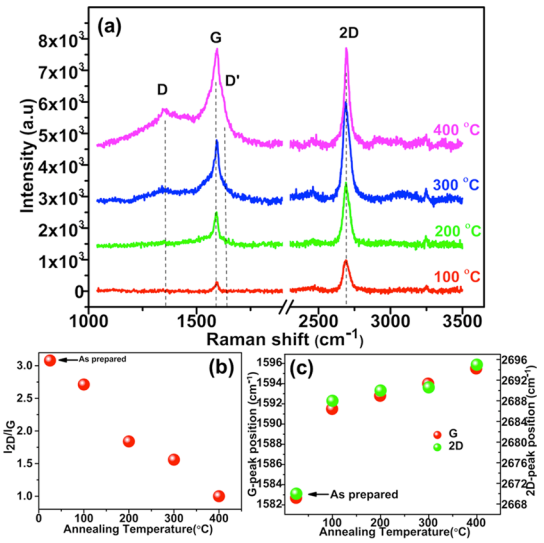

Figure 3. Raman analysis of LFG-Au4 samples as a function of annealing temperatures: (a) overlay of Raman spectra; (b) change in I_{2D}/I_G ratio; (c) change in G and 2D position.

the Au film (as discussed earlier). This crack formation allows localized strain relaxation at the LFG-Au interface to a small extent. The pre-existing cracks in the Au film in our case act as edges and defects, thereby accelerating the hole-growth process. Hole growth occurs by retraction of the edges; that is, the material flux from the edge is transported in directions away from the crack, leading to a withdrawal resulting in wire-like strands. The self-diffusion due to a Rayleigh-plateau-like instability then breaks these wire-like strands into spherules.[46]

The plasmonic activity of the LFG-Au4 films as a function of temperature under which the Au nanoparticles were formed is further investigated by their SERS performance, as shown in Figure 3a. The EF determined at the G band after annealing to 100 °C dramatically decreases to ∼0.5. With further annealing, the EF increases gradually to reach a maximum of 5.5 at 400 °C. While the 2D intensity band steadily increased with rising temperatures, the G band along with band splitting displays a significant enhancement in the intensity equaling the 2D band intensity at 400 °C (see Supporting Information S3). Both enhanced intensity and splitting in the G band indicate significant interaction between graphene and AuNPs owing to graphene conforming around the AuNPs due to thermal annealing.

Figure 3b shows changes in the I_{2D}/I_G ratio of the LFG-Au4 films before and after annealing. The I_{2D}/I_G of the as-prepared LFG-Au4 film decreases from 3.1 to 0.9 after annealing to 400 °C. This decrease in I_{2D}/I_G indicates the possibility of LFG doped with Au. Additionally the position of the G and the 2D bands of the annealed LFG-Au4 films blue-shifted with respect to the as-prepared samples from 1582 to 1596 cm^{-1} and 2670 to 2694 cm^{-1}, respectively, as seen in Figure 3c.

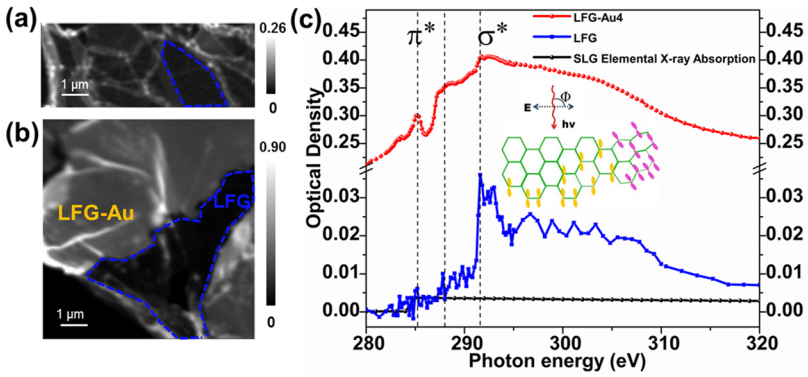

Figure 4. (a, b) Optical density (OD) images of LFG and as-prepared LFG-Au4 samples. (c) Spatially resolved C K-edge NEXAFS spectra of the LFG (blue) and as-prepared LFG-Au4 (red) extracted from their respective OD mapping and calculated elemental X-ray absorption for SLG (black). (Inset) Schematic of in-plane circularly polarized X-rays incident on SLG.

The variation in I_{2D}/I_G ratio and shifts in the G and 2D bands are related to doping in graphene, in agreement with the previous studies.[21,48] A similar trend in I_{2D}/I_G has been observed in metal−graphene structures supported on Si/SiO_2 substrates.[30] Furthermore, blue-shift of both the G and 2D bands can be related to p-doping of graphene, as the type of doping can be determined from the position shifts of G and 2D bands, respectively.[19,21,48] It is known that blue-shift (phonon stiffening) of the G band and red-shift (phonon softening) of the 2D band indicate n-type doping, while simultaneous blue-shift of both the G and 2D bands depicts p-type doping of graphene.[19,48] Upon doping, the Fermi surface is altered, shifting the Kohn anomaly from $q = 0$ due to the difference in the charge concentration, resulting in the E_{2g} phonon stiffening.[18,19] Also, DFT calculations by Giovanetti *et al*. have shown that changes in the Fermi level due to graphene−metal interaction driven by work function differences cause either n-type (graphene-Al, Ag, Cu) or p-type doping (graphene-Au, Pt).[49] The enhanced LFG-Au interaction resulting in Fermi level shift (p-doping) is consistent with both the theoretical calculations and experimental observations. Additionally, emergence of small D, D′, and D+D′ bands at 1350, 1620, and 2900 cm^{-1} indicates a small increase in disorder, which we attribute to wrinkles formed in graphene at the AuNPs edges.

Additionally, at lower annealing temperatures (100 °C), the EF for LFG-Au4 samples decreases compared to the as-prepared samples, indicating the disappearance of near-field confinement; however the EF is enhanced with increasing annealing temperatures. The SEM images (Figure 2a,b) show the increased intercrack distances, which results in diminishing near-field confinement. Thus, we expect that the EF observed after annealing is predominantly due to plasmons inherent to graphene; nonetheless contributions from Au surface plasmons still exist. The increase in EF at larger interparticulate distance suggests the minimal role of localized surface plasmon resonators (SPRs) due to interactions between Au nanoparticles.[28] At 400 °C the AuNPs are not only separated further from each other but get wrapped with LFG (schematically shown in Figure 2f,h and SEM images 2g,i). This wrapping of graphene over AuNPs enhances the interaction between the two materials, leading to p-type doping of LFG, thus causing an electronic and chemical inhomogeneity in the suspended LFG. These electronically modified localized areas of LFG form graphene SPRs (G-SPRs). The areas with the graphene-AuNPs and regions without AuNPs form seamless interconnectivities, resulting in SERS enhancement.

The chemical and electronic inhomogeneity across LFG, due to graphene−Au wrapping and the localized graphene−Au interfacial interaction, is further probed by synchrotron-based nano-spectro-microscopic technique.

STXM Mapping of the Localized Electronic Structure of LFG-Au Plasmonic System. Figure 4a,b shows the integrated C K-edge STXM image of the LFG and LFG-Au4 sample between 280 and 320 eV photon energies. The gray scale represents the absolute OD distribution. Distinct regions with different ODs are clearly identified, and the spectroscopic details of the demarked regions were obtained using the aXis2000 analysis package.[50] The OD data are obtained by converting the transmission data considering the I/I_o ratio, where I is the transmitted photon flux through the sample and I_o the incident flux, measured at a clear region, free of sample. The spatially resolved near-edge X-ray absorption fine structure (NEXAFS) C K-edge spectra of the LFG and as-prepared LFG-Au4 are extracted from the OD mapping. The samples show a π^* transition at 285 eV and a broad σ^* resonance at 291.5 eV. The extracted NEXAFS spectra provide a detailed spatial map of specific unoccupied electronic states such as the π^* and the σ^* above the Fermi level along with the pre-edge. The positions, relative intensities, shapes, and line widths of these resonances can be used to understand the local chemical and electronic structure of the material under study.

The combination of spatial and spectral resolution that is available from STXM makes the technique ideal to understand materials at the nanoscale, including graphene.

The STXM data were acquired employing an elliptically polarized undulator (EPU) that allows tunable polarization. Depending on the angle of the electric field vector (*E*) of the incident polarized X-ray beam with respect to the molecular orientation, relative intensities of π^* and σ^* resonances can be determined. In SLG, a network of six-membered ring structures, the π^* orbitals (constituting the C $2p_z$ orbitals) are oriented perpendicular to the basal plane, while the σ^* orbitals are localized along the basal plane. Thus, when *E* is parallel to the basal planes, the intensity of the σ^* resonance is maximum, and the π^* resonance maximum is more likely when the *E* is perpendicular to the basal planes.[51] In our experiments during the acquisition of STXM data, the incident circularly polarized X-ray beam is normal to the sample surface, *i.e.*, π^* orbitals, and accordingly should result in only a maximum σ^* and no π^* resonance.

On comparing the NEXFAS spectra in Figure 4c, the LFG (blue) shows a negligibly small π^* resonance, while the LFG-Au4 (red) exhibits a prominent π^* peak that is sharp and fairly smooth. This could be due to small corrugations caused by the biaxial strain as seen in the Raman spectra (Figure 1c). These small topographical changes in the large area (40×40 μm) result in the angling of the π^* orbitals with respect to the basal planes, leading to increased intensities of the same (inset schematic in Figure 4c). On the contrary, the negligibly small π^* intensity in the LFG indicates that it is uniform at flat regions. With the high spatial resolution of STXM, subtle changes in the homogeneity of the films can be easily detected. Because the LFG film is ultrathin, the noise level in the spectra is quite significant. The peak(s) between the π^* and σ^* resonances, *i.e.*, 287−289 eV, previously ascribed as the interlayer state were later proved to be due to residual functionalization, mostly C−H and −C═O bondings.[52−54] The absence of peaks in this region for the LFG sample indicates the graphene is clean from the transfer process. However, after the deposition of Au, broader peaks between 287 and 289 eV are discernible, indicating the presence of various functional groups/moieties, which could originate from adsorbed moisture from the ambient or other sources.

Thinnest Graphene Measured. There have been very few reports of the OD mapping of SLG by the spectromicroscopic technique.[54,43] On the basis of the variation of the OD, regions and layers with discrete thickness from the sample of interest can be determined. In our case the thickness of LFG is monitored by considering the difference in the pre- and postedge of the extracted NEXAFS spectra from the OD mapping; here the edge-step OD of LFG, ∼0.007, is determined. This is close to the theoretically calculated edge-step OD of SLG, ∼0.004, as shown in black in Figure 4c (for details see the Supporting Information). To the best of our knowledge, this is the smallest OD experimentally measured for a single graphene layer thus far.

For further understanding of the graphene−metal interfacial interaction we examined the spatially resolved C K-edge OD maps of LFG-Au4 annealed at 400 °C. Figure 5a shows the integrated C K-edge OD image of LFG-Au4 at 400 °C between 280 and 320 eV photon energies. We observe four regions with different AuNP distributions and refer to them as region-1 to region-4. Region-1, the dark region, is the overlying LFG sheet; regions-2 and -3, the bright clusters and brighter patches, correspond to smaller clusters of AuNPs and self-assembled AuNP aggregates underneath the LFG. Region-4, individual bright spots, corresponds to the homogeneously dispersed uniformly sized circular AuNPs. Figure 5b is the color composite mapping of the distinct regions (*i.e.*, regions-1−4) from OD mapping (Figure 5a), which was created by combining individual component maps from distinctive regions using the principal component analysis (PCA) from the PCA_GUI software (http://xray1.physics.sunysb.edu/data/software.php). The purple zone (region-1) corresponds to areas of the LFG that are mostly flat and completely devoid of AuNPs; the yellow zone (region-2) corresponds to smaller areas in the vicinity of isolated and/or fewer AuNPs; the green zone (region-3) relates to larger clusters or patches of AuNPs; and the red spots (region-4) are the localized area of the isolated AuNPs. The blue region corresponds to the empty region intentionally chosen for the I_o measurement. The SEM micrograph (Figure 5c) of the same region as the OD mapping after the STXM measurement shows no change to the LFG film.

Average NEXAFS spectra for the distinctly demarcated regions of Figure 5b are shown in Figure 5d. The spectra show a noticeable difference in the relative π^* intensities with no change in the energy of peak positions, accompanied by a pre-edge feature between 283 and 285 eV, which is quite distinct for region-4. The NEXAFS spectra from various regions are compared with the as-prepared LFG spectrum (black) for reference. The variation in π^* intensities in the annealed LFG-Au4 at 400 °C film is due to changes in the LFG morphology from the varying size and distribution of AuNPs. The NEXAFS spectrum (pink) for region-1, area of LFG that is free from AuNPs, shows a small π^* intensity compared to the as-prepared LFG with no π^* peak, indicative of corrugations arising from the surrounding AuNPs even in the flat region. The π^* intensity (yellow and green for regions-2, -3) further increases for areas with larger particle distributions.

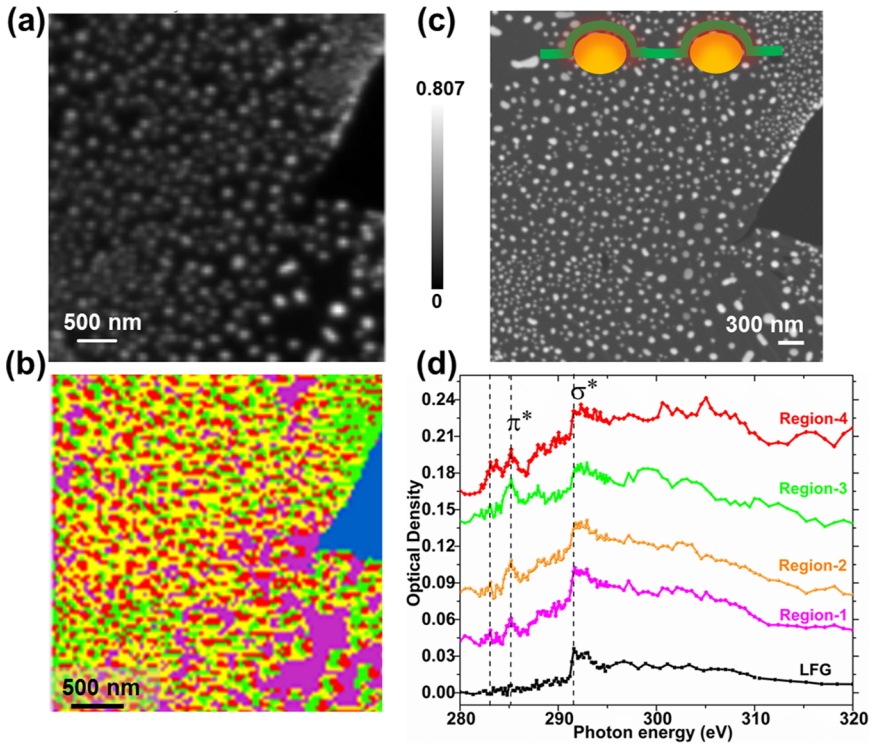

Figure 5. (a) Average OD of LFG-Au4 @400 °C sample between 280 and 320 eV. (b) Color composite mapping of the π^* resonance from the OD mapping using the PCA. (c) SEM image of the same region after STXM measurement. (d) Spatially resolved color-coded C K-edge NEXAFS spectra extracted from the respective regions in average OD mapping (b) and reference LFG (black) spectrum.

The π^* peak, which was sharp and smooth for the as-prepared LFG-Au4 (Figure 4c), now appears to be split, although not distinctly into individual peaks, which we relate to the hybridization between graphene C $2p_z$ orbitals and Au d orbitals. The C K-edge spectra (red) from region-4 is most interesting due to the fact that they arise from individual isolated AuNPs that are wrapped with graphene, resulting in strong graphene–metal interfacial interactions. Also, observed in this spectrum is the presence of a strong pre-edge peak at ~283–284 eV, below the π^* resonance. The origin of the pre-edge peak, unique to graphene, has been strongly debated, initially claimed to be due to disorder or defect-induced localized states[55] and later to a signature dispersionless interlayer state.[52] Previously, for graphite and single-walled carbon nanotubes intercalated with $FeCl_3$ the pre-edge peak has been associated with lowering of the Fermi level (E_F) induced by charge transfer.[49] In our case the pre-edge emerges only after annealing and is very prominent for region-4. Accordingly, we relate this to the charge transfer between graphene and Au, as the graphene conforms around the AuNPs, resulting in strong interaction between the two at the interface. Similar pre-edge and π^* resonances previously observed in SLG on Cu and Ni substrates have been assigned to graphene metal hybridization,[53] the extent of which strongly depended on the interfacial distance between the two as theoretically predicted.[49]

CONCLUSIONS

In the as-prepared (at RT) LFG-Au samples, SERS enhancement is mainly due to the near-field confinement from the nanocracks between the metal islands in the Au film. The enhanced intensity of the D, G, and 2D Raman bands validates the SERS enhancement in graphene due to the Au-SPR. Further, the red-shift of the 2D band coupled with the emergence of a prominent π^* peak in the LFG-Au films indicates strain-induced corrugations in the sample due to gold deposition. The overall enhancement of the peaks in the LFG-Au film and the absence of a pre-edge peak in the NEXAFS C K-edge spectra strongly associated with charge transfer and weak orbital mixing in both LFG and LFG-Au samples clearly indicate a relatively weak interaction between the LFG and Au. This is in agreement with the literature.[49]

Upon annealing (100–300 °C), the initial enhancement due to the near-field confinement diminishes with the increased interparticle distance. At 400 °C, the interaction between LFG and Au is greatly enhanced, as corroborated by a significant increase in G band intensity. Furthermore, blue-shift of the Raman modes and the pre-edge peak between 283 and 284 eV in the NEXAFS spectrum of the sample treated at 400 °C appears due to graphene enveloping the Au-NPs, elucidating the lowering of the E_F (p-doping) with increased doping levels. Also, the splitting of the π^*

resonance, although not as explicit and strong as previously observed,[53] indicates a stronger localized graphene−Au interfacial interaction. This leads to graphene surface plasmon resonance; that is, the surface plasmon in graphene and the Au overlap further, enhancing the charge transfer between graphene and the metal. This validates the gradual increase in the enhancement factor with the annealing, in particular at 400 °C (shown in Figure 6).

The enhanced interaction between AuNPs and graphene leads to p-type doping in LFG, causing an electronic and chemical inhomogeneity in the suspended LFG. Manjavacas *et al*. using numerical modeling have shown that addition of an electron to the nanoislands of graphene can activate plasmonic frequencies that were previously absent.[56] Recent research on numerical simulation of the surface plasmon polariton propagation in periodically perturbed SLG (generated by chemical or electrostatic gating) predicts the formation of graphene-based plasmonic metamaterials.[57−59] In this study, seamlessly interconnected chemically/electronically unaltered and altered regions of LFG and LFG-Au form a short-range-ordered 2D metamaterial, inducing strong electromagnetic fields in the graphene−AuNPs hybrid nanostructure. This induced electromagnetic field is observed in the form of graphene-SPRs.

In conclusion, two distinct enhancement phenomena observed in freestanding graphene−Au films are reported. First, enhancement through the metal nanogaps *via* graphene and, second, through strong interactions between thermally formed AuNPs and LFG, leading to a unique graphene surface plasmon resonance. The localized graphene−Au interaction at the nanoscale is reported using STXM for the first time. Additionally, the measured ~0.007 OD of LFG, in good agreement with the theoretically calculated edge jump, is the smallest OD experimentally observed thus far. We believe that our findings on these hybrid plasmonic nanostructures can pave the way for future fabrication of graphene-based plasmonic devices with unique configurations and enhanced properties for a wide range of applications.

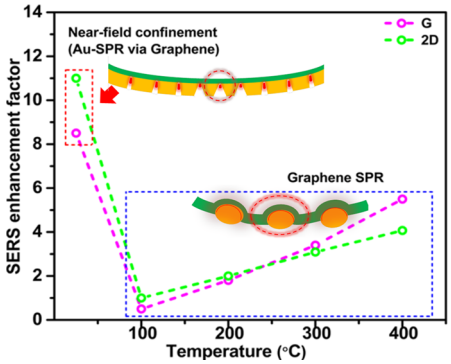

Figure 6. Calculated enhancement factor (EF), considering the ratio of SERS spectra and normal Raman spectra, of the LFG-Au4 sample before and after annealing.

MATERIALS AND METHODS

Materials. *Sample Preparation.* Single-layer graphene on copper samples (synthesized by chemical vapor deposition (CVD)) used in this study was purchased from Graphene Supermarket. Large-area freestanding SLG samples are prepared by wet chemical etching of the underlying Cu using 0.1 M ammonium persulfate solution followed by multiple rinsing in DI water. The LFG sample(s) is (are) then transferred onto Au-coated TEM grid(s) (3 mm, 400 mesh company SPI, 433HG-CF), each perforation of size 40 μm × 40 μm.

Large-Area LFG-Au Plasmonic System. To fabricate large-area, freestanding plasmonic system, we followed a two-step approach. First, a gold film of two different thicknesses, 4 and 8 nm, is deposited on SLG/Cu samples by vacuum thermal evaporation (10^{-5} Torr), at the rate of 0.5 nm/min, monitored by a thickness monitor. The Cu substrate is etched off as described earlier, and freestanding LFG-Au films are prepared such that the SLG is atop Au. Second, LFG-Au4 and LFG-Au8 samples are annealed at 100, 200, 300, and 400 °C in a CVD furnace in argon ambient for 5 min to create Au nanoparticles. A shorter annealing time of 5 min was chosen to prevent breaking of the freestanding LFG/Au films.

Materials Characterization. *Scanning Electron Microscopy.* The SEM micrographs of LFG, LFG-Au4, and LFG-Au8 samples before and after thermal annealing were obtained using the ZEISS EVO 50 at SyLMAND beamline of the Canadian Light Source Inc. (CLSI) synchrotron facility.

Raman Spectroscopy. Raman spectra were recorded using 532 nm excitation on a Renishaw 2000 system at the Mid-IR beamline of CLSI. A 50× objective and 1800 line/mm grating were used for the measurement. Short accumulation times and low power (~2.5 mW) were used to avoid localized heating from the laser.

Scanning Transmission X-ray Microscopy. The STXM measurements were carried out at the Spectromicroscopy (SM) beamline at CLSI. The beamline is equipped with an elliptically polarized undulator source, with a 25 nm outermost Fresnel's zone plate providing 30 nm spatial resolution. The incoming X-ray beam (I_o) from a plane grating monochromator is focused into a spot by the Fresnel's zone plate with an order sorting aperture that allows only the first order, filtering the rest. The sample was raster-scanned with synchronized detection of transmitted X-rays to generate an image sequence (stacks) over a range of photon energies. STXM data were analyzed using aXis2000 (available at http://unicorn.mcmaster.ca/aXis2000.html). The collected image sequence from the region of interest (ROI) was first aligned and then converted to optical density by using the incident flux (I_o) spectrum that was collected adjoining the ROI during the measurement. The color composite mapping was generated from the average OD image by combining individual component maps using PC analysis, and the corresponding C K-edge NEXAFS spectra were derived from the respective regions.

High-Resolution Transmission Electron Microscopy (HRTEM). The HRTEM measurements were carried out at the Electron Microscopy Centre, NDSU, Fargo, ND, USA. The HRTEM images of the LFG-Au4 (400 °C) were obtained with a JEOL JEM-200CX II operated at 200 kV using a lanthanum hexaboride emitter and collected using a GATAN Orius SC1000 bottom-mount CCD, and images were processed with Gatan digital micrograph software. Preliminary studies were carried out for the LFG-Au4 samples, and regions with Au nanoparticles were selectively chosen.

Conflict of Interest: The authors declare no competing financial interest.

Acknowledgment. Research described in this paper was performed at the Spectromicroscopy (SM), SyLMAND, and Mid-IR beamlines of the Canadian Light Source, which is funded by the Canada Foundation for Innovation, the Natural Sciences and Engineering Research Council of Canada, the National Research Council Canada, the Canadian Institutes of Health Research, the Government of Saskatchewan, Western Economic Diversification Canada, and the University of Saskatchewan. We acknowledge the SM beamline staff, Dr. C. Karunakaran, and Mr. Y. Lu for their extended help at the beamline; Mr. J. Maley and Dr. X. Liu for their help with the Raman measurements; and Ms. S. Purdy at the Physics Department, University of Saskatchewan, for the help with sample annealing.

Supporting Information Available: Schematic of the LFG film, SEM image of the suspended LFG-Au4 film, before and after annealing; SEM images of the morphological transformation of the LFG-Au8 film upon annealing, the splitting of the G band of the annealed (400 °C) LFG-Au4 film; HRTEM image of LFG-Au4 film; NEXAFS spectra and other relevant data are presented. This material is available free of charge *via* the Internet at http://pubs.acs.org.

REFERENCES AND NOTES

1. Novoselov, K. S.; Geim, A. K.; Morozov, S. V.; Jiang, D.; Katsnelson, M. I.; Grigorieva, I. V.; Dubonos, S. V.; Firsov, A. A. Two-Dimensional Gas of Massless Dirac Fermions in Graphene. *Nature* **2005**, *438*, 197–200.
2. Novoselov, K. S.; Geim, A. K.; Morozov, S. V.; Jiang, D.; Zhang, Y.; Dubonos, S. V.; Grigorieva, I. V.; Firsov, A. A. Electric Field Effect in Atomically Thin Carbon Films. *Science* **2004**, *306*, 666–669.
3. Bonaccorso, F.; Sun, Z.; Hasan, T.; Ferrari, A. C. Graphene Photonics and Optoelectronics. *Nat. Photonics* **2010**, *4*, 611–622.
4. Grigorenko, A. N.; Polini, M.; Novoselov, K. S. Graphene Plasmonics. *Nat. Photonics* **2012**, *6*, 749–758.
5. Zhou, W.; Lee, J.; Nanda, J.; Pantelides, S. T.; Pennycook, S. J.; Idrobo, J. C. Atomically Localized Plasmon Enhancement in Monolayer Graphene. *Nat. Nanotechnol.* **2012**, *7*, 161–165.
6. Bostwick, A.; Speck, F.; Seyller, T.; Horn, K.; Polini, M.; Asgari, R.; MacDonald, A. H.; Rotenberg, E. Observation of Plasmarons in Quasi-Freestanding Doped Graphene. *Science* **2010**, *328*, 999–1002.
7. Yan, H. G.; Low, T.; Zhu, W. J.; Wu, Y. Q.; Freitag, M.; Li, X. S.; Guinea, F.; Avouris, P.; Xia, F. N. Damping Pathways of Mid-Infrared Plasmons in Graphene Nanostructures. *Nat. Photonics* **2013**, *7*, 394–399.
8. Koppens, F. H. L.; Chang, D. E.; de Abajo, F. J. G. Graphene Plasmonics: A Platform for Strong Light-Matter Interactions. *Nano Lett.* **2011**, *11*, 3370–3377.
9. Low, T.; Avouris, P. Graphene Plasmonics for Terahertz to Mid-Infrared Applications. *ACS Nano* **2014**, *8*, 1086–1101.
10. García de Abajo, F. J. Graphene Plasmonics: Challenges and Opportunities. *ACS Photonics* **2014**, *1*, 135–152.
11. Fei, Z.; Rodin, A. S.; Andreev, G. O.; Bao, W.; McLeod, A. S.; Wagner, M.; Zhang, L. M.; Zhao, Z.; Thiemens, M.; Domniguez, G.; *et al.* Gate-Tuning of Graphene Plasmons Revealed by Infrared Nano-Imaging. *Nature* **2012**, *487*, 82–85.
12. Chen, J. N.; Badioli, M.; Alonso-Gonzalez, P.; Thongrattanasiri, S.; Huth, F.; Osmond, J.; Spasenovic, M.; Centeno, A.; Pesquera, A.; Godignon, P.; *et al*. Optical Nano-Imaging of Gate-Tunable Graphene Plasmons. *Nature* **2012**, *487*, 77–81.
13. Emani, N. K.; Chung, T.-F.; Ni, X.; Kildishev, A. V.; Chen, Y. P.; Boltasseva, A. Electrically Tunable Damping of Plasmonic Resonances with Graphene. *Nano Lett.* **2012**, *12*, 5202–5206.
14. Mousavi, S. H.; Kholmanov, I.; Alici, K. B.; Purtseladze, D.; Arju, N.; Tatar, K.; Fozdar, D. Y.; Suk, J. W.; Hao, Y.; Khanikaev; *et al*. Inductive Tuning of Fano-Resonant Metasurfaces Using Plasmonic Response of Graphene in the Mid-Infrared. *Nano Lett.* **2013**, *13*, 1111–1117.
15. Brar, V. W.; Jang, M. S.; Sherrott, M.; Lopez, J. J.; Atwater, H. A. Highly Confined Tunable Mid-Infrared Plasmonics in Graphene Nanoresonators. *Nano Lett.* **2013**, *13*, 2541–2547.
16. Ferrari, A. C.; Basko, D. M. Raman Spectroscopy as a Versatile Tool for Studying the Properties of Graphene. *Nat. Nanotechnol.* **2013**, *8*, 235–246.
17. Ferrari, A. C.; Meyer, J. C.; Scardaci, V.; Casiraghi, C.; Lazzeri, M.; Mauri, F.; Piscanec, S.; Jiang, D.; Novoselov, K. S.; Roth, S.; *et al*. Raman Spectrum of Graphene and Graphene Layers. *Phys. Rev. Lett.* **2006**, *97*, 187401.
18. Ferrari, A. C. Raman Spectroscopy of Graphene and Graphite: Disorder, Electron-Phonon Coupling, Doping and Nonadiabatic Effects. *Solid State Commun.* **2007**, *143*, 47–57.
19. Pisana, S.; Lazzeri, M.; Casiraghi, C.; Novoselov, K. S.; Geim, A. K.; Ferrari, A. C.; Mauri, F. Breakdown of the Adiabatic Born-Oppenheimer Approximation in Graphene. *Nat. Mater.* **2007**, *6*, 198–201.
20. Wang, Q. H.; Jin, Z.; Kim, K. K.; Hilmer, A. J.; Paulus, G. L. C.; Shih, C.-J.; Ham, M.-H.; Sanchez-Yamagishi, J. D.; Watanabe, K.; Taniguchi, T.; *et al*. Understanding and Controlling the Substrate Effect on Graphene Electron-Transfer Chemistry *via* Reactivity Imprint Lithography. *Nat. Chem.* **2012**, *4*, 724–732.
21. Shi, Y. M.; Dong, X. C.; Chen, P.; Wang, J. L.; Li, L. J. Effective Doping of Single-Layer Graphene from Underlying SiO_2 Substrates. *Phys. Rev. B* **2009**, *79*, 115402.
22. Huang, M. Y.; Yan, H. G.; Chen, C. Y.; Song, D. H.; Heinz, T. F.; Hone, J. Phonon Softening and Crystallographic Orientation of Strained Graphene Studied by Raman Spectroscopy. *Proc. Natl. Acad. Sci. U.S.A.* **2009**, *106*, 7304–7308.
23. Huang, M. Y.; Yan, H. G.; Heinz, T. F.; Hone, J. Probing Strain-Induced Electronic Structure Change in Graphene by Raman Spectroscopy. *Nano Lett.* **2010**, *10*, 4074–4079.
24. Lee, J. E.; Ahn, G.; Shim, J.; Lee, Y. S.; Ryu, S. Optical Separation of Mechanical Strain from Charge Doping in Graphene. *Nat. Commun.* **2012**, *3*, 1024.
25. Zabel, J.; Nair, R. R.; Ott, A.; Georgiou, T.; Geim, A. K.; Noyoselov, K. S.; Casiraghi, C. Raman Spectroscopy of Graphene and Bilayer under Biaxial Strain: Bubbles and Balloons. *Nano Lett.* **2012**, *12*, 617–621.
26. Lee, J. U.; Yoon, D.; Cheong, H. Estimation of Young's Modulus of Graphene by Raman Spectroscopy. *Nano Lett.* **2012**, *12*, 4444–4448.
27. Casiraghi, C.; Hartschuh, A.; Qian, H.; Piscanec, S.; Georgi, C.; Fasoli, A.; Novoselov, K. S.; Basko, D. M.; Ferrari, A. C. Raman Spectroscopy of Graphene Edges. *Nano Lett.* **2009**, *9*, 1433–1441.
28. Schedin, F.; Lidorikis, E.; Lombardo, A.; Kravets, V. G.; Geim, A. K.; Grigorenko, A. N.; Novoselov, K. S.; Ferrari, A. C. Surface-Enhanced Raman Spectroscopy of Graphene. *ACS Nano* **2010**, *4*, 5617–5626.
29. Lee, J.; Shim, S.; Kim, B.; Shin, H. S. Surface-Enhanced Raman Scattering of Single- and Few-Layer Graphene by the Deposition of Gold Nanoparticles. *Chem.—Eur. J.* **2011**, *17*, 2381–2387.
30. Lee, J.; Novoselov, K. S.; Shin, H. S. Interaction between Metal and Graphene: Dependence on the Layer Number of Graphene. *ACS Nano* **2010**, *5*, 608–612.
31. Xu, W.; Xiao, J.; Chen, Y.; Chen, Y.; Ling, X.; Zhang, J. Graphene-Veiled Gold Substrate for Surface-Enhanced Raman Spectroscopy. *Adv. Mater.* **2013**, *25*, 928–933.
32. Xu, W.; Ling, X.; Xiao, J.; Dresselhaus, M. S.; Kong, J.; Xu, H.; Liu, Z.; Zhang, J. Surface Enhanced Raman Spectroscopy on a Flat Graphene Surface. *Proc. Natl. Acad. Sci. U.S.A.* **2012**, *109*, 9281–9286.
33. Xu, G. W.; Liu, J. W.; Wang, Q.; Hui, R. Q.; Chen, Z. J.; Maroni, V. A.; Wu, J. Plasmonic Graphene Transparent Conductors. *Adv. Mater.* **2012**, *24*, Op71–Op76.
34. Heeg, S.; Fernandez-Garcia, R.; Oikonomou, A.; Schedin, F.; Narula, R.; Maier, S. A.; Vijayaraghavan, A.; Reich, S. Polarized Plasmonic Enhancement by Au Nanostructures Probed through Raman Scattering of Suspended Graphene. *Nano Lett.* **2013**, *13*, 301–308.

35. Wang, P.; Zhang, W.; Liang, O.; Pantoja, M.; Katzer, J.; Schroeder, T.; Xie, Y.-H. Giant Optical Response from Graphene–Plasmonic System. *ACS Nano* **2012**, *6*, 6244–6249.
36. Gan, X.; Mak, K. F.; Gao, Y.; You, Y.; Hatami, F.; Hone, J.; Heinz, T. F.; Englund, D. Strong Enhancement of Light–Matter Interaction in Graphene Coupled to a Photonic Crystal Nanocavity. *Nano Lett.* **2012**, *12*, 5626–5631.
37. Wang, Y. Y.; Ni, Z. H.; Shen, Z. X.; Wang, H. M.; Wu, Y. H. Interference Enhancement of Raman Signal of Graphene. *Appl. Phys. Lett.* **2008**, *92*, 043121.
38. Gao, L. B.; Ren, W. C.; Liu, B. L.; Saito, R.; Wu, Z. S.; Li, S. S.; Jiang, C. B.; Li, F.; Cheng, H. M. Surface and Interference Coenhanced Raman Scattering of Graphene. *ACS Nano* **2009**, *3*, 933–939.
39. Ling, X.; Zhang, J. Interference Phenomenon in Graphene-Enhanced Raman Scattering. *J. Phys. Chem. C* **2011**, *115*, 2835–2840.
40. Waldmann, D.; Butz, B.; Bauer, S.; Englert, J. M.; Jobst, J.; Ullmann, K.; Fromm, F.; Ammon, M.; Enzelberger, M.; Hirsch, A.; *et al*. Robust Graphene Membranes in a Silicon Carbide Frame. *ACS Nano* **2013**, *7*, 4441–4448.
41. Nair, R. R.; Blake, P.; Grigorenko, A. N.; Novoselov, K. S.; Booth, T. J.; Stauber, T.; Peres, N. M. R.; Geim, A. K. Fine Structure Constant Defines Visual Transparency of Graphene. *Science* **2008**, *320*, 1308.
42. Henke, B. L. G.; E, M.; Davis, J. C. X-ray Interactions: Photoabsorption, Scattering, Transmission and Reflection at E = 50−30,000 eV, Z=1−92. *At. Data Nucl. Data Tables* **1993**, *54*, 181–342.
43. Zhou, J. G.; Wang, J.; Sun, C. L.; Maley, J. M.; Sammynaiken, R.; Sham, T. K.; Pong, W. F. Nano-Scale Chemical Imaging of a Single Sheet of Reduced Graphene Oxide. *J. Mater. Chem.* **2011**, *21*, 14622–14630.
44. Berciaud, S.; Ryu, S.; Brus, L. E.; Heinz, T. F. Probing the Intrinsic Properties of Exfoliated Graphene: Raman Spectroscopy of Free-Standing Monolayers. *Nano Lett.* **2009**, *9*, 346–352.
45. Mohiuddin, T. M. G.; Lombardo, A.; Nair, R. R.; Bonetti, A.; Savini, G.; Jalil, R.; Bonini, N.; Basko, D. M.; Galiotis, C.; Marzari, N.; *et al*. Uniaxial Strain in Graphene by Raman Spectroscopy: G Peak Splitting, Gruneisen Parameters, and Sample Orientation. *Phys. Rev. B* **2009**, *79*, 205433.
46. Thompson, C. V. Solid-State Dewetting of Thin Films. *Annu. Rev. Mater. Res.* **2012**, *42*, 399–434.
47. Petryayeva, E.; Krull, U. J. Localized Surface Plasmon Resonance: Nanostructures, Bioassays and Biosensing—A Review. *Anal. Chim. Acta* **2011**, *706*, 8–24.
48. Das, A.; Pisana, S.; Chakraborty, B.; Piscanec, S.; Saha, S. K.; Waghmare, U. V.; Novoselov, K. S.; Krishnamurthy, H. R.; Geim, A. K.; Ferrari, A. C.; *et al*. Monitoring Dopants by Raman Scattering in an Electrochemically Top-Gated Graphene Transistor. *Nat. Nanotechnol.* **2008**, *3*, 210–215.
49. Giovannetti, G.; Khomyakov, P. A.; Brocks, G.; Karpan, V. M.; van den Brink, J.; Kelly, P. J. Doping Graphene with Metal Contacts. *Phys. Rev. Lett.* **2008**, *101*, 026803.
50. Hitchcock, A. Analysis of X-ray Microscopy Images and Spectra, 2013; http://unicorn.mcmaster.ca/aXis2000.html.
51. Abbas, G.; Papakonstantinou, P.; Iyer, G. R. S.; Kirkman, I. W.; Chen, L. C. Substitutional Nitrogen Incorporation through RF Glow Discharge Treatment and Subsequent Oxygen Uptake on Vertically Aligned Carbon Nanotubes. *Phys. Rev. B* **2007**, *75*, 195429.
52. Pacile, D.; Papagno, M.; Rodriguez, A. F.; Grioni, M.; Papagno, L. Near-Edge X-ray Absorption Fine-Structure Investigation of Graphene. *Phys. Rev. Lett.* **2008**, *101*, 066806.
53. Lee, V.; Park, C.; Jaye, C.; Fischer, D. A.; Yu, Q. K.; Wu, W.; Liu, Z. H.; Pei, S. S.; Smith, C.; Lysaght, P.; *et al*. Substrate Hybridization and Rippling of Graphene Evidenced by Near-Edge X-ray Absorption Fine Structure Spectroscopy. *J. Phys. Chem. Lett.* **2010**, *1*, 1247–1253.
54. Schultz, B. J.; Patridge, C. J.; Lee, V.; Jaye, C.; Lysaght, P. S.; Smith, C.; Barnett, J.; Fischer, D. A.; Prendergast, D.; Banerjee, S. Imaging Local Electronic Corrugations and Doped Regions in Graphene. *Nat. Commun.* **2011**, *2*, 372.
55. Pereira, V. M.; Guinea, F.; dos Santos, J. M. B. L.; Peres, N. M. R.; Neto, A. H. C. Disorder Induced Localized States in Graphene. *Phys. Rev. Lett.* **2006**, *96*, 036801.
56. Manjavacas, A.; Thongrattanasiri, S.; de Abajo, F. J. G. Plasmons Driven by Single Electrons in Graphene Nanoislands. *Nanophotonics (Berlin, Ger.)* **2013**, *2*, 139–151.
57. Vakil, A.; Engheta, N. Transformation Optics Using Graphene. *Science* **2011**, *332*, 1291–1294.
58. Bludov, Y. V.; Peres, N. M. R.; Vasilevskiy, M. I. Graphene-Based Polaritonic Crystal. *Phys. Rev. B* **2012**, *85*, 245409.
59. Silveiro, I.; Manjavacas, A.; Thongrattanasiri, S.; de Abajo, F. J. G. Plasmonic Energy Transfer in Periodically Doped Graphene. *New J. Phys.* **2013**, *15*, 033042.